APPLIED SCIENCES AND ENGINEERING

Piezoelectric ultrasound energy–harvesting device for deep brain stimulation and analgesia applications

Tao Zhang[1]†, Huageng Liang[2]†, Zhen Wang[3], Chaorui Qiu[4], Yuan Bo Peng[3], Xinyu Zhu[1], Jiapu Li[1], Xu Ge[1], Jianbo Xu[1], Xian Huang[2], Junwei Tong[2], Jun Ou-Yang[1], Xiaofei Yang[1], Fei Li[4]*, Benpeng Zhu[1]*

Supplying wireless power is a challenging technical problem of great importance for implantable biomedical devices. Here, we introduce a novel implantable piezoelectric ultrasound energy–harvesting device based on Sm-doped $Pb(Mg_{1/3}Nb_{2/3})O_3$-$PbTiO_3$ (Sm-PMN-PT) single crystal. The output power density of this device can reach up to 1.1 W/cm^2 in vitro, which is 18 times higher than the previous record (60 mW/cm^2). After being implanted in the rat brain, under 1-MHz ultrasound with a safe intensity of 212 mW/cm^2, the as-developed device can produce an instantaneous effective output power of 280 µW, which can immediately activate the periaqueductal gray brain area. The rat electrophysiological experiments under anesthesia and behavioral experiments demonstrate that our wireless-powered device is well qualified for deep brain stimulation and analgesia applications. These encouraging results provide new insights into the development of implantable devices in the future.

INTRODUCTION

With the rapid development of the biomicroelectronics, implantable biomedical devices have emerged and attracted considerable attention (1–3). These devices exhibit numerous advantages in improving the quality of patient life and/or extending patient life, although supplying power to these devices is still a technical challenge. Deep brain stimulation (DBS) as a powerful tool has been clinically used to treat Parkinson's disease (4), essential tremor (5), dystonia (6), pain (7), and other diseases (8–10). However, its power supply remains a main challenge (11–17), as shown in fig. S1. The traditional scheme of an outer power resource requires transcutaneous or percutaneous wires that are cumbersome and prone to infection, especially for long-term application (18). Integration of the battery with the implants is another choice, but the battery must be replaced regularly because of its limited energy capacity, bringing postoperative pain and financial burdens to patients (19).

Recently, to address this issue, magnetoelectric and ultrasonic wireless energy-harvesting technologies have been proposed (20, 21). Compared to electromagnetic waves, ultrasound (US) can realize a longer travel depth and a better spatial resolution in the tissue (22). Furthermore, according to the U.S. Food and Drug Administration's regulation, the safety threshold of US in the human body is 720 mW/cm^2 (23), which is dozens of times greater than that of radio waves (10 mW/cm^2) (24). These two factors enable ultrasonic wireless energy-harvesting technology's unique advantages in biomedical applications in contrast to other wireless power transmission technologies, such as electromagnetic (25–27), piezoelectric (20, 21), triboelectric (28–30), electrostatic (31–33), biofuel cell (34, 35), thermoelectric (36, 37), and photovoltaic (38, 39) (table S1).

Because the ZnO nanowire array was successfully driven by US to produce continuous electrical output in 2007 (40), many efforts have been conducted to develop piezoelectric US energy–harvesting (PUEH) devices (41–45). The state-of-the-art devices made from polyvinylidene fluoride, lead zirconate titanate (PZT) film, PZT 1-3 composite, and potassium-sodium niobate 1-3 composite exhibit very low energy density in the range of 3.75 µW/cm^2 to 60 mW/cm^2 (table S2) in vitro (41–45). Because of this, no PUEH devices have been used in in vivo experiments over the years. Theoretically, the output can be enhanced by increasing US's intensity, but the US's intensity must not exceed the safety threshold; otherwise, damage to the body will be induced by heat as a result of the US. Thus, it is highly desired to enhance the output energy density by improving the energy-harvesting efficiency of PUEH devices.

Here, we design a miniature (13.5 mm by 9.6 mm by 2.1 mm) and flexible PUEH device with 6 × 6 elements using Sm-doped $Pb(Mg_{1/3}Nb_{2/3})O_3$-$PbTiO_3$ (Sm-PMN-PT) single crystals, whose piezoelectric coefficient (d_{33}), electromechanical coupling coefficient (k_{33}), and relative permittivity (ε) are up to 4000 pC/N, 95%, and 13,000 (46), respectively. This Sm-PMN-PT single crystal–based PUEH device (abbreviated as Sm-PUEH device) can produce an instantaneous output power up to 1.1 W/cm^2 and an average charging power of 4270 ± 40 nW in vitro, which are much higher than the previous record values (60 mW/cm^2, 160 nW) (43, 45). Furthermore, under 1-MHz US with a safe intensity (212 mW/cm^2), such a device can produce an instantaneous effective output power up to 280 µW in vivo. According to the results of rat experiments both in an anesthetized and an awake state, we demonstrate that this Sm-PUEH device has the capability (table S3) to realize DBS and immediately activate the periaqueductal gray (PAG) to reach the aim of analgesia.

RESULTS AND DISCUSSION

Principle and design of Sm-PUEH device

In our design, we propose the Sm-PUEH device be implanted subcutaneously for DBS (Fig. 1A). According to the principle of PUEH device (47, 48), the output power (P) is related to the piezoelectric material's dielectric coefficient ($ε_{33}$), effective elastic coefficient(c_{33}),

[1]School of Optical and Electronic Information, Huazhong University of Science and Technology, Wuhan 430074, China. [2]Department of Urology, Union Hospital of Tongji Medical College, Huazhong University of Science and Technology, Wuhan 430022, China. [3]Department of Psychology, University of Texas at Arlington, Arlington, TX 76019, USA. [4]Electronic Materials Research Lab, Key Lab of Education Ministry/International Center for Dielectric Research, School of Electronic and Information Engineering, State Key Laboratory for Mechanical Behavior of Materials, Xi'an Jiaotong University, Xi'an 710049, China.
*Corresponding author. Email: benpengzhu@hust.edu.cn (B.Z.); ful5@xjtu.edu.cn (F.L.)
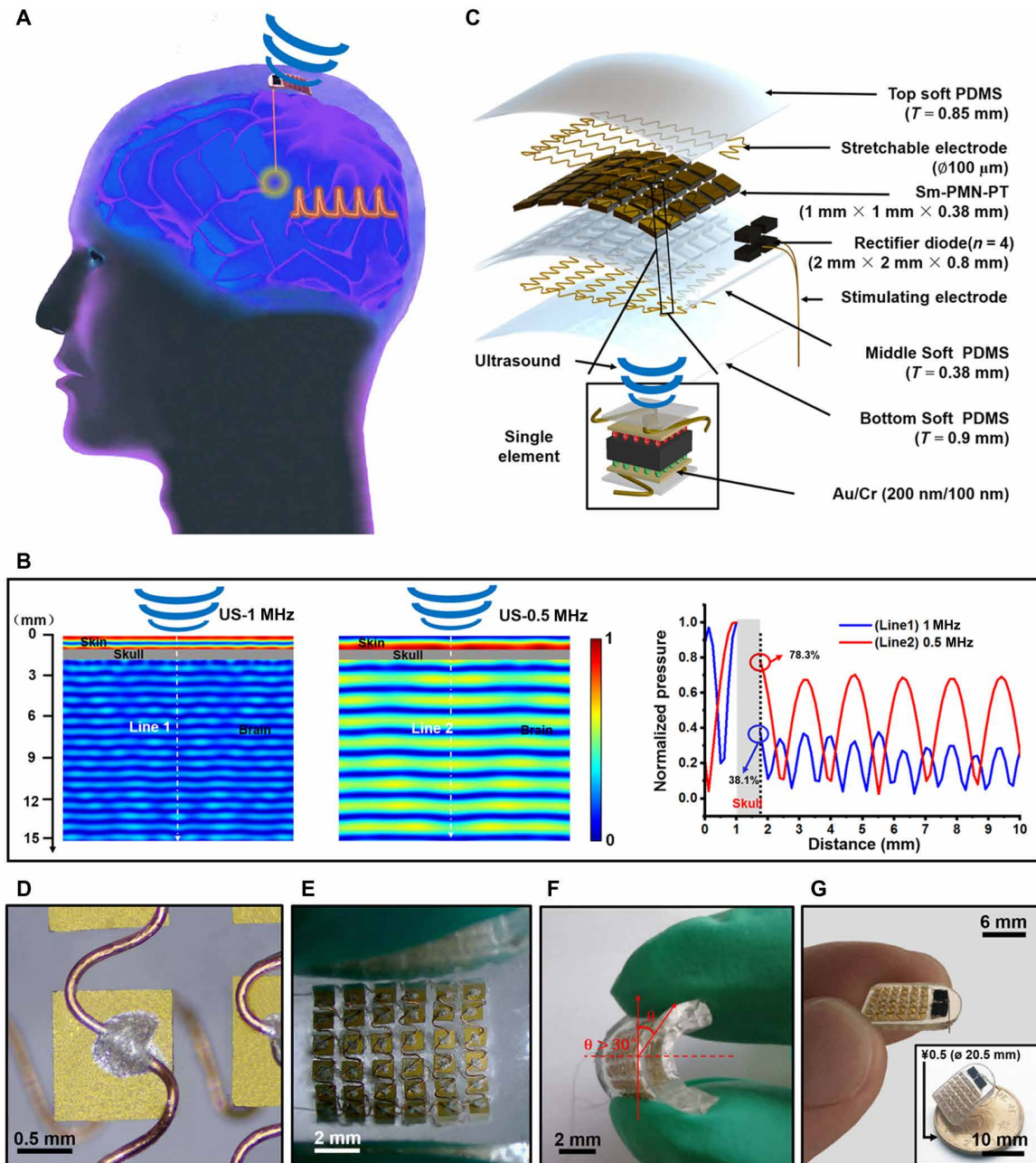†These authors contributed equally to this work.

Fig. 1. Schematic diagram and design of the flexible Sm-PUEH device. (**A**) Schematic diagram of the Sm-PUEH device designed for DBS and analgesia. DI, deionized. (**B**) Attenuation of US after penetrating through the brain as a function of distance with different frequencies (0.5 and 1 MHz). (**C**) Exploded view of Sm-PUEH device, consisting of soft polydimethylsiloxane (PDMS), stretchable copper electrodes, Sm-PMN-PT, rectifier diodes, and stimulating electrodes (from side to center). (**D**) The stretchable electrical connection for the device. (**E**) The flexible device in a bent state. (**F**) Side view of the flexible device with bending angle greater than 30°. (**G**) Optical image of the obtained device held with fingers. The inset shows that the device is smaller than a coin of ¥0.5 (20.5 mm in diameter).

and electromechanical coupling coefficient (k_{33}), which can be expressed as (note S1)

$$P \propto \frac{\varepsilon_{33}}{c_{33}} \frac{1}{\left(k_{33} + \frac{1}{k_{33}}\right)^2} \quad (1)$$

Considering that the value of k_{33} is in the range of 0 to 1, the formula $\frac{1}{\left(k_{33} + \frac{1}{k_{33}}\right)^2}$ is a monotonically increasing function. One

method to improve the output power of the device is to choose the piezoelectric material with high electromechanical coupling factor and high dielectric permittivity. Thus, we chose Sm-PMN-PT single crystal as the active material for our proposed PUEH device. The relevant parameters of Sm-PMN-PT crystal are shown in table S4. As reported in previous literature (49, 50), kilohertz-range US can propagate through the skull and activate cranial nerves. After penetrating through the skull (table S5) (51), as presented in Fig. 1B, 0.5-MHz US can maintain 78.3% of the input pressure; only 38.1%

pressure remains for 1-MHz US. Therefore, to avoid the influence of US direct stimulation, the operating frequency of our Sm-PUEH device is designed to be 1 MHz. Figure 1C illustrates an exploded view of our Sm-PUEH device. Sm-PMN-PT single crystal is lapped down to the thickness of 380 μm and then cut into small pieces with the size of 1 mm by 1 mm (fig. S2). These elements are connected with stretchable electrodes (52, 53) (Fig. 1D) to form a 6 × 6 array and embedded in soft polydimethylsiloxane (PDMS) with excellent biocompatibility (fig. S3) and stretchability (54, 55). The whole device can be regarded as 36 minicurrent sources in parallel (fig. S4). The specific fabrication process of Sm-PUEH device is shown in fig. S5. Moreover, it exhibits good flexibility with a bent angle more than 30° under external force (Fig. 1, E and F). The entire device with the weight of 0.78 g is 13.5 mm long, 9.6 mm wide, and 2.1 mm thick (fig. S6), which is smaller than a coin of ¥0.5 (20.5 mm in diameter) (Fig. 1G).

Electrical output characteristics of Sm-PUEH device

To explore the electrical output characteristics of our Sm-PUEH device, a test system was built as described in Fig. 2 (A and B). According to the impedance spectrum (fig. S7), the resonant frequency of each Sm-PMN-PT element is approximately 1 MHz. To ensure that the Sm-PUEH device works at this resonant frequency, the applied US in this experiment is set to be 1 MHz (fig. S8). The device's output voltage under 1-MHz US with different intensities was measured (Fig. 2C and fig. S9). The output voltage is positively correlated with the intensity of the input pulse US. Saturation occurs when the input sound pressure is higher than 2.5 MPa, and the open-circuit voltage can reach more than 80 peak-to-peak voltage (movie S1). In addition, US incident angle and the bending state of the device may affect the output efficiency. We investigated the dependence of the device's output voltage on the US incident angle or bending situation (Fig. 2D and movies S2 and S3). The output
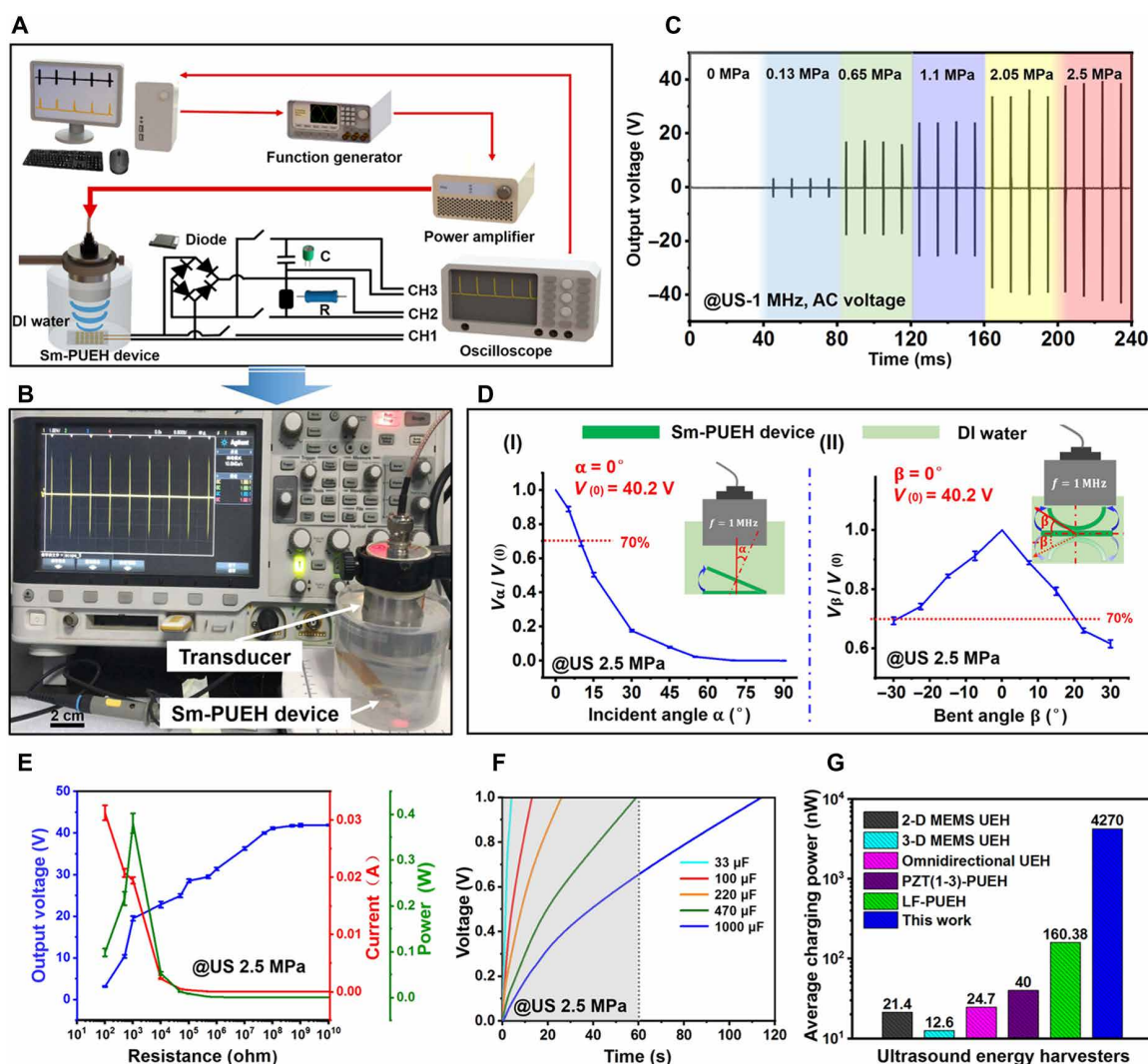

Fig. 2. Electrical output characteristics of Sm-PUEH device. (**A**) Schematic diagram of electrical output test system for the Sm-PUEH device. (**B**) Sm-PUEH device in the test. (**C**) The output voltage signal of Sm-PUEH device measured under 1-MHz US with different intensities. (**D**) The output voltage signal of Sm-PUEH device at different US incident angles (I) and at different bending angles (II). (**E**) The output voltage, current, and power of Sm-PUEH device under different load conditions driven by a pulse US with 2.5 MPa. (**F**) Charging curves of various capacitors (33, 100, 220, 470, and 1000 μF) with Sm-PUEH device driven by a pulse US with 2.5 MPa. (**G**) Comparison of average charging power with different US energy harvesters. 2-D, two-dimensional; MEMS, Micro-Electro-Mechanical System.

open-circuit voltage decreased with the US incident angle increasing; when the angle was greater than 45°, the output voltage tended to be 0. In a bending situation, the output open-circuit voltage diminished slowly with the rise of the bending angle. If the US incident angle was less than 10° or the bending angle was less than 20°, then the device can maintain 70% output.

Figure 2E presents the change of output voltage (blue), current (red), and power (green) for the Sm-PUEH device in an external load resistance range from 100 ohm to 10 gigohm. As the load resistance increases, the output voltage keeps raising until saturation at high resistance (>100 megohm). With a load resistance of 1 kilohm, the maximum instantaneous power is calculated to be 0.4 W, where the output voltage and current are 20 V and 0.02 A, respectively. The instantaneous output power density can reach up to 1.1 W/cm^2, which is 18 times higher than the previous record (60 mW/cm^2) (43). The voltage produced by PUEH device takes the form of AC pulses, which cannot be directly used for DBS. Therefore, the AC signals should be converted into DC output by a rectifier circuit (fig. S10). After rectification, the device's output voltage is shown in fig. S11, which shows that the relationship between the voltage output and the US intensity is similar to that in Fig. 2C. Moreover, the pulse width of the output voltage is consistent with that of the applied US (fig. S12).

As presented in Fig. 2F, five different energy storage capacitors (33, 100, 220, 470, and 1000 μF) are charged under US (2.5 MPa). Less than 60 s are required for a 470-μF capacitor to be charged to 1 V (movie S4). The calculation formula of average charging power is given below (31)

$$\overline{P} = \frac{C_s V^2}{2T} \tag{2}$$

where C_s is the capacitance, T is the charging time, and V is the stored voltage. When Sm-PUEH device charges a 1000-μF capacitor (fig. S13), its output power is determined to be 4270 ± 40 nW, which is 26 times larger than the previous record (160 nW) (45). Figure 2G shows that PUEHs are superior to electrostatic US energy harvesters (31, 56, 57) in terms of charging power, and among them, Sm-PUEH is the best one (table S6). We attribute this excellent charging energy efficiency to the performance of Sm-PMN-PT single crystal and the desired structure of the device. Together with three 220-μF capacitors in parallel, 56 commercial blue light-emitting diodes (LEDs) can be illuminated simultaneously within 5 min by our Sm-PUEH device (fig. S14 and movie S5). The Sm-PUEH device can directly light up a blue LED connecting a 220-μF capacitor in parallel (fig. S15 and movie S6). The outstanding output performance of the device mainly lies in the high-performance piezoelectric Sm-PMN-PT single crystal. Furthermore, the resonant working state (1 MHz) of the device and the array structure (6 × 6) contribute to the improvement of output power.

Output characteristics in tissue of Sm-PUEH device
Before the DBS experiment, it was necessary to test the output characteristics of the device in tissue under biological safety. The device was placed under the pork tissue in vitro, the thickness of which was 30 mm, including 1 mm of skin, 11 mm of fat, and 18 mm of muscle (Fig. 3A). Driven by 1-MHz US with intensity of 0.65 MPa, the Sm-PUEH device can still produce an output of 7.7 V [Fig. 3B (I) and movie S7]. Although this output voltage is just 46% of the value

(16.6 V) tested in deionized (DI) water, it is high enough for the proposed application and is a record for a PUEH device. When the device was placed under the skin, the output voltage was measured to be 9.3 V, 56% of 16.6 V. We also studied the relationship between the voltage output and the US incident angle. When the US incident angle is less than 15°, the open-circuit voltage can remain 4.7 V [Fig. 3B (II)]. All tested results showed that the device can show excellent output performance in biological tissues.

To eliminate the influence of temperature change on nerve stimulation, we established a different US stimulation strategy (Fig. 3C) and tested the device's temperature change both in air [Fig. 3D (I)] and in tissue [Fig. 3D (II)]. There are three strategies for applying US with a pulse repetition frequency (PRF): (I) No US, no US is applied; (II) US 3 s, 1-MHz US (US-400 c/p, PRF = 50 Hz, 0.65 MPa) irradiating for 3 s; (III) US 5 min, 1-MHz US (US-400 c/p, PRF = 50 Hz, 0.65 MPa) irradiating for 5 min with an interval (on 3 s and off 3 s). The results indicate that our US strategy never caused substantial temperature change not only in air but also in tissue (Fig. 3E).

As reported in (58), the charge on a stimulating electrode may cause electrolysis, which is harmful. To identify a safe stimulation frequency for Sm-PUEH device, we investigated electrolysis, where the stimulating electrode (monophasic) was immersed in normal saline when the device was driven by 1-MHz US with different PRFs (Fig. 3F). The specific parameters of the applied US are shown in table S7. Once a bubble appears, the water is electrolyzed. In Fig. 3G, the blue area represents safe condition, while electrolysis occurs in the red area. According to our results, the irradiation of 1-MHz US with PRF of 50 Hz for 3 s is safe for an in vivo experiment; the irradiation of 1-MHz US with PRF of 120 Hz for 3 s will lead to electrolysis.

The PAG activation by Sm-PUEH device
Pain seriously endangers people's health and quality of life and causes a huge economic burden to society (59–62). Usually, drug chemotherapy can relieve pain, but widely used analgesics have an additional risk of death (63, 64). Theoretically, the PAG is a key brain region involving the pain inhibition descending pathway, and there are mounting evidences demonstrating that DBS to the PAG is a promising alternative for analgesia (65–69).

To explore the feasibility of the Sm-PUEH device for DBS and toward analgesia application, we designed and conducted an experiment of the PAG activation. As depicted in Fig. 4A, our device was implanted under the scalp of a rat, and the stimulating and recording electrodes were both placed in the PAG brain area. Under an applied 1-MHz US of 212 mW/cm^2 (US-400 c/p, PRF = 50 Hz, 0.65 MPa), the Sm-PUEH device exhibits an instantaneous output power up to 400 μW (approximate voltage, 2 V; current, 200 μA) and the effective power is about 280 μW, as shown in Fig. 4B. Figure 4C describes the recorded signal of the electrophysiological experiment under two different conditions: US and no device, and US and device. Only when the device is driven by US can the periodic variations of local field potential (LFP) of the PAG be recorded. In addition, when the stimulated signal's amplitude is increased or its duration is elevated, the amplitude of the recorded signal is enhanced; meanwhile, its waveform has no obvious change (fig. S16). It is worth noting that the frequency of the PAG activation is equal to the PRF of the applied pulse US (Fig. 4C). When the US's PRF is adjusted to 25 or 100 Hz, a similar phenomenon can be observed (Fig. 4D), suggesting that the activities of the PAG can be precisely controlled by this Sm-PUEH device.
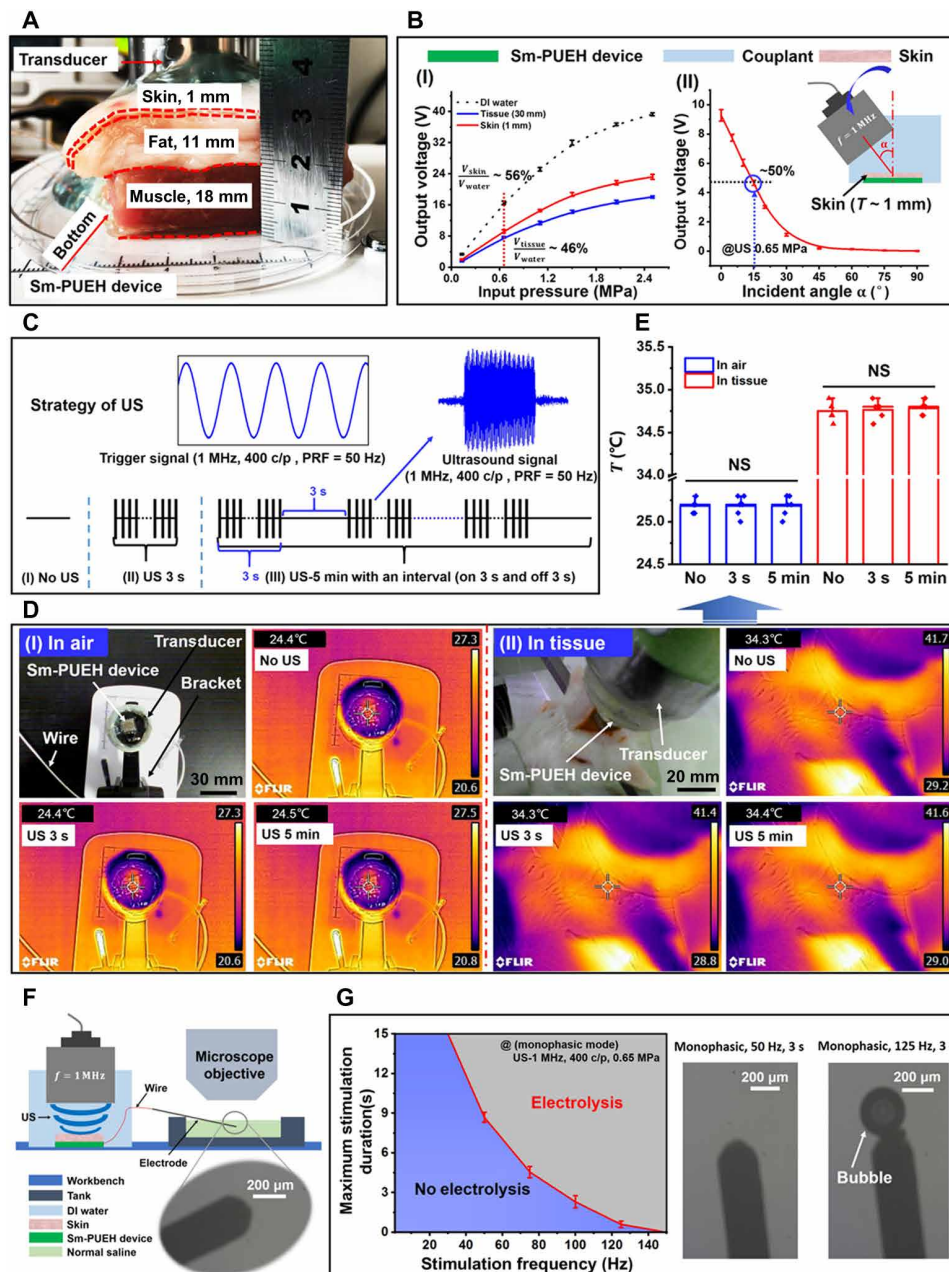
Fig. 3. Output characteristics in tissue of Sm-PUEH device. (**A**) Schematic diagram of experimental testing of the device in pork tissue. (**B**) The output voltage of the device in pork with a thickness of 30 mm driven by the pulse US of different intensities (I) and the output characteristics of the device covered with 1-mm-thick skin by applying different US incident angles (II). (**C**) Schematic diagram of the strategy for applying US: (I) No US, no US is applied; (II) US 3 s, 1-MHz US [US-400 c/p, pulse repetition frequency (*PRF*) = 50 Hz, 0.65 MPa] irradiating for 3 s; (III) US 5 min, 1 MHz US (US-400 c/p, *PRF* = 50 Hz, 0.65 MPa) irradiating for 5 min with an interval (on 3 s and off 3 s). (**D**) The device's temperature change in the air and the tissue. (**E**) The comparison of temperature change for the three groups. NS, not significant. (**F**) Schematic diagram of electrolysis experiment of Sm-PUEH device. (**G**) Maximum stimulation duration for Sm-PUEH device in monophasic operation determined by time of electrolysis on an electrode in normal saline, as evidenced by gas bubbles (*n* = 4).

Electrophysiological experiments (LFP recordings) in rats under anesthesia

To demonstrate the capability of our Sm-PUEH device for analgesia application, we carried out an in vivo electrophysiological study on rats under anesthesia (Fig. 5A). For the establishment of a pain animal mode, 50 μl of 3% formalin solution was injected into the rat's left hindpaw. This formalin-induced pain can last for 60 min. LFP activities from the spinal cord dorsal horn (L5) involve in not only receiving primary afferent signals from the periphery but also recognizing descending inputs from supraspinal sources. According to previous literature (*70*, *71*), the measurement of electrophysiological signals from spinal cord dorsal horn can be used to quantify responses to noxious stimuli. Consequently, we placed a recording electrode in the spinal cord to detect the LFP activities of
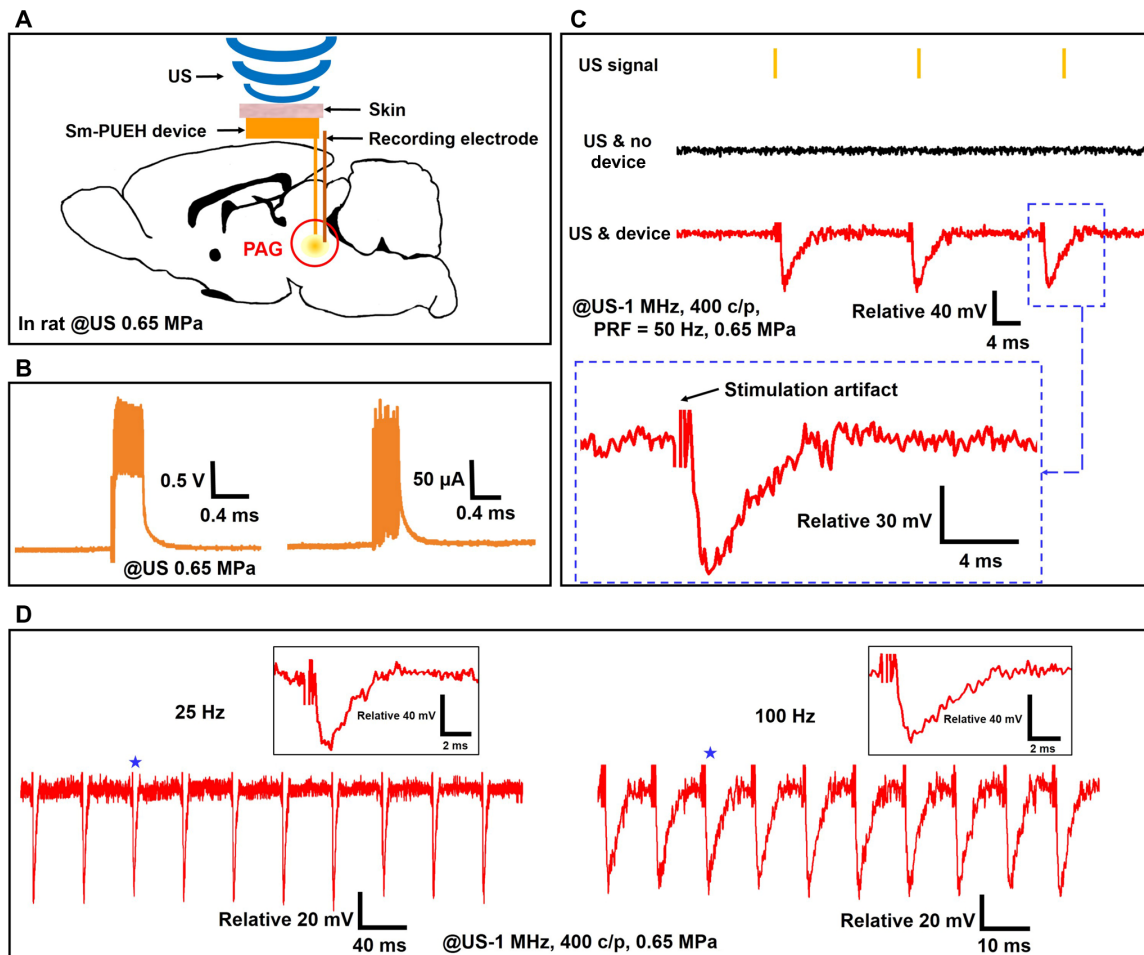
Fig. 4. The PAG activation by Sm-PUEH device. (**A**) Schematic diagram of in vivo experimental design of DBS using Sm-PUEH device implanted in rats, where the stimulation electrode is placed in the PAG brain area (7 mm posterior to the bregma, 0.5 mm lateral to the midline, 5.5 mm deep), and the recording electrode is near the stimulation electrode. (**B**) Voltage and current measurement in the brain tissue. (**C**) In vivo recorded local field potential (LFP) signal (stimulus artifacts cropped for clarity) under a 1-MHz US (US-400 c/p, *PRF* = 50 Hz, 0.65 MPa) without implanted device (US & no device), and with implanted device (US & device). (**D**) In vivo recorded PAG activities by Sm-PUEH device stimulation with *PRF* of 25 Hz (left) and 100 Hz (right) (stimulus artifacts cropped for clarity). Insets (indicated by stars) show the zoom-in of individual LFP.

dorsal horn. Meanwhile, the Sm-PUEH device was implanted under the scalp of the rat for the purpose of stimulating the PAG. In our experiment, there were two groups: the stimulation group ($n = 8$) and the control group ($n = 8$). For the former, as shown in Fig. 5B, at the 30th min after formalin injection, 1-MHz US (US-400 c/p, *PRF* = 50 Hz, 0.65 MPa) began to irradiate for 5 min with an interval (on 3 s and off 3 s), while for the latter group, no US was applied.

Figure 5C shows the LFP activity changes in both the stimulation group and the control group. The record data (data were imported into Spike2 for offline analysis) and the waveforms of different frequency bands are referred to fig. S17. We analyzed the waveform and power spectrum (0 to 100 Hz) of the recorded data. Evidently, power spectrum intensity increased in both groups after formalin injection, which means that the LFP activities of dorsal horn were enhanced and the rat began to feel pain. When the US irradiated, i.e., the PAG stimulation by the Sm-PUEH device occurred, power spectrum intensity decreased immediately, implying that the LFP activities of dorsal horn decreased and formalin-induced pain was alleviated. Once the US turned off, dorsal horn returned to the situation of LFP activity enhancement. For the

control group, no obvious changes of LFP activity were observed. The heatmap of the power spectrum ratio also illustrates that LFP activities in delta, theta, alpha, beta, and gamma waves decreased significantly under the PAG stimulation by the Sm-PUEH device (Fig. 5D). For delta waves, significant differences were observed between the control group and the stimulation group during the 30th to 35th min ($P < 0.001$), 35th to 36th min ($P < 0.01$), and 36th to 40th min ($P < 0.05$) (Fig. 5E). Similar results were detected in the theta, alpha, beta, and gamma bands (fig. S18).

Behavioral experiments

To further verify the feasibility of our Sm-PUEH device for analgesia application, we conducted rat behavioral experiments (Fig. 6A). As shown in Fig. 6 (B to D), our device is fully implanted in rat's brain under the scalp, and the rat can recover from surgery and move freely after 10 days. In this experiment, the rats are still divided into the stimulation group ($n = 6$) and the control group ($n = 6$), and the stimulation strategy is consistent with that in electrophysiological experiment (Fig. 6E). After formalin injection, the rat mainly has three kinds of behavior responses: paw down [Fig. 6F (I)],
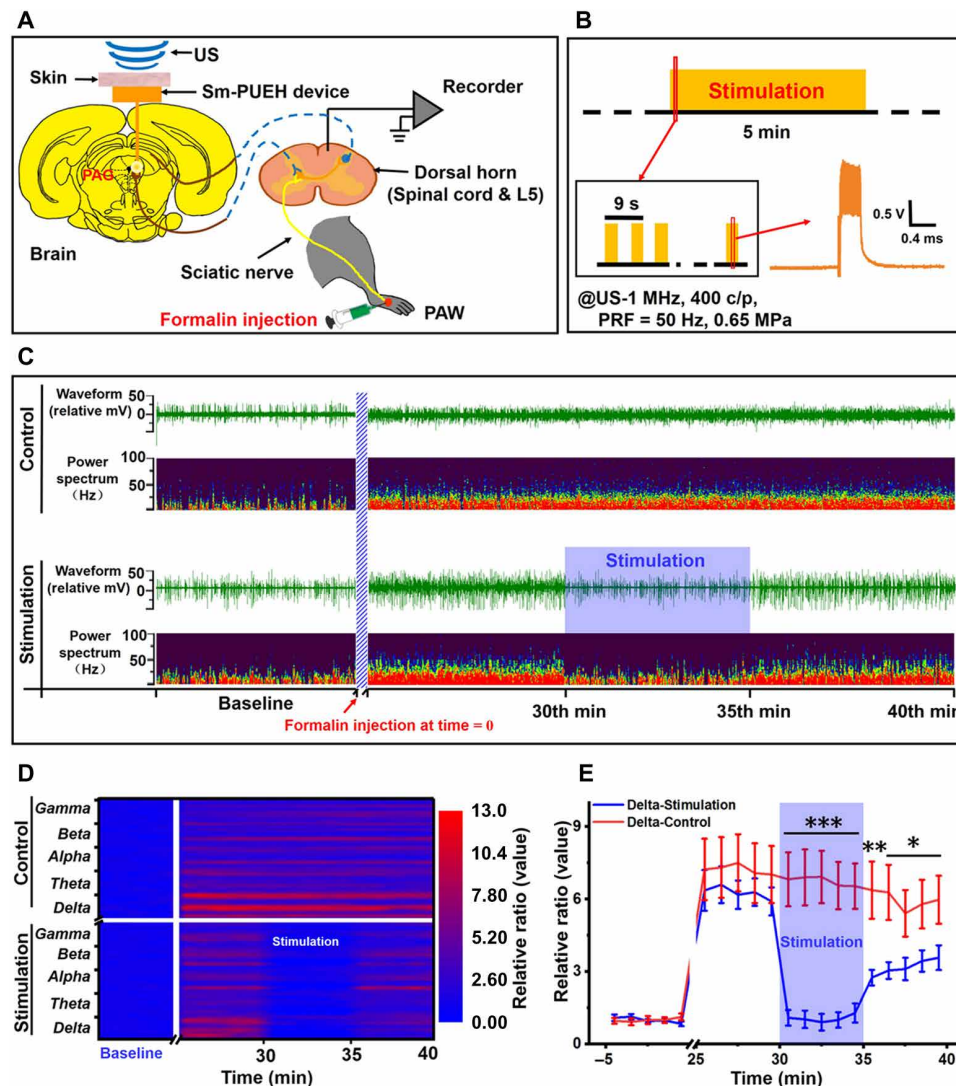
Fig. 5. Inhibition of LFP activity of spinal cord dorsal horn by Sm-PUEH device's PAG stimulation. (**A**) Schematic diagram of the experimental design. Three-percent formalin (50 μl) is injected into the left hindpaw, and US is then applied to trigger the PAG stimulation by the Sm-PUEH device. Electrophysiological signals of the spinal cord dorsal horn (L5) are recorded. (**B**) Schematic diagram of stimulation strategy with US (US-400 c/p, *PRF* = 50 Hz, 0.65 MPa) for 5 min with an interval (on 3 s and off 3 s). (**C**) Representative example of LFP activities from the spinal cord dorsal horn (L5) between the control group (top) and the stimulation group (bottom). In each group, the first row represents the raw trace (waveform), and the second row demonstrates power spectrum. Formalin is injected at time = 0. (**D**) Heatmap comparison of the power spectrum ratio (calculated by baseline) between the control group and the stimulation group. The power spectrum is broken down into delta (0 to 3 Hz) wave, theta (4 to 7 Hz) wave, alpha (8 to 12 Hz) wave, beta (13 to 30 Hz) wave, and gamma (31 to 100 Hz) wave. (**E**) The comparison of power spectrum changes in delta (0 to 3 Hz) wave between the control group ($n = 8$) and the stimulation group ($n = 8$). The power spectrum is calculated by the average of each minute, and ratio (*y* axis) is processed by the average baseline of the first 5 min. All data are presented as means ± SEM. *$P < 0.05$, **$P < 0.01$, and ***$P < 0.001$ versus control group.

paw up [Fig. 6F (II)], and paw licking [Fig. 6F (III)]. Figure 6G illustrates the weighted score of formalin-induced pain for these two groups. At the 30th min, their scores reached a peak value simultaneously. Once the US began to irradiate and this PAG stimulation by the Sm-PUEH device occurs, the pain score of the stimulation group dropped significantly. However, for the control group, the score remained at its maximum. We also counted the duration of paw up and paw licking from 30th to 35th min (Fig. 6H). Evidently, there was also a significant reduction in the total time of paw up ($P < 0.001$) and paw licking ($P < 0.05$) in the stimulation group (movie S8). The observations in the behavioral experiment are in good agreement with the results of the electrophysiological experiment

(under anesthesia). All of these promising results demonstrate that this implanted Sm-PUEH device exhibits an excellent performance on the PAG stimulation–produced analgesia. Furthermore, no obvious adverse reaction (movie S9) and surrounding tissue damage (fig. S3) were observed after long-term implantation in rats, which indicates considerable biocompatibility of our device.

In summary, we introduced a miniature (13.4 mm by 9.6 mm by 2.1 mm) and flexible PUEH device with 6 × 6 elements using the Sm-doped Sm-PMN-PT single crystals with ultrahigh piezoelectric and dielectric properties. In vitro, this Sm-PUEH device can produce an instantaneous output power up to 1.1 W/cm^2 and an average charging power to 4270 ± 40 nW, which are about 18 times and
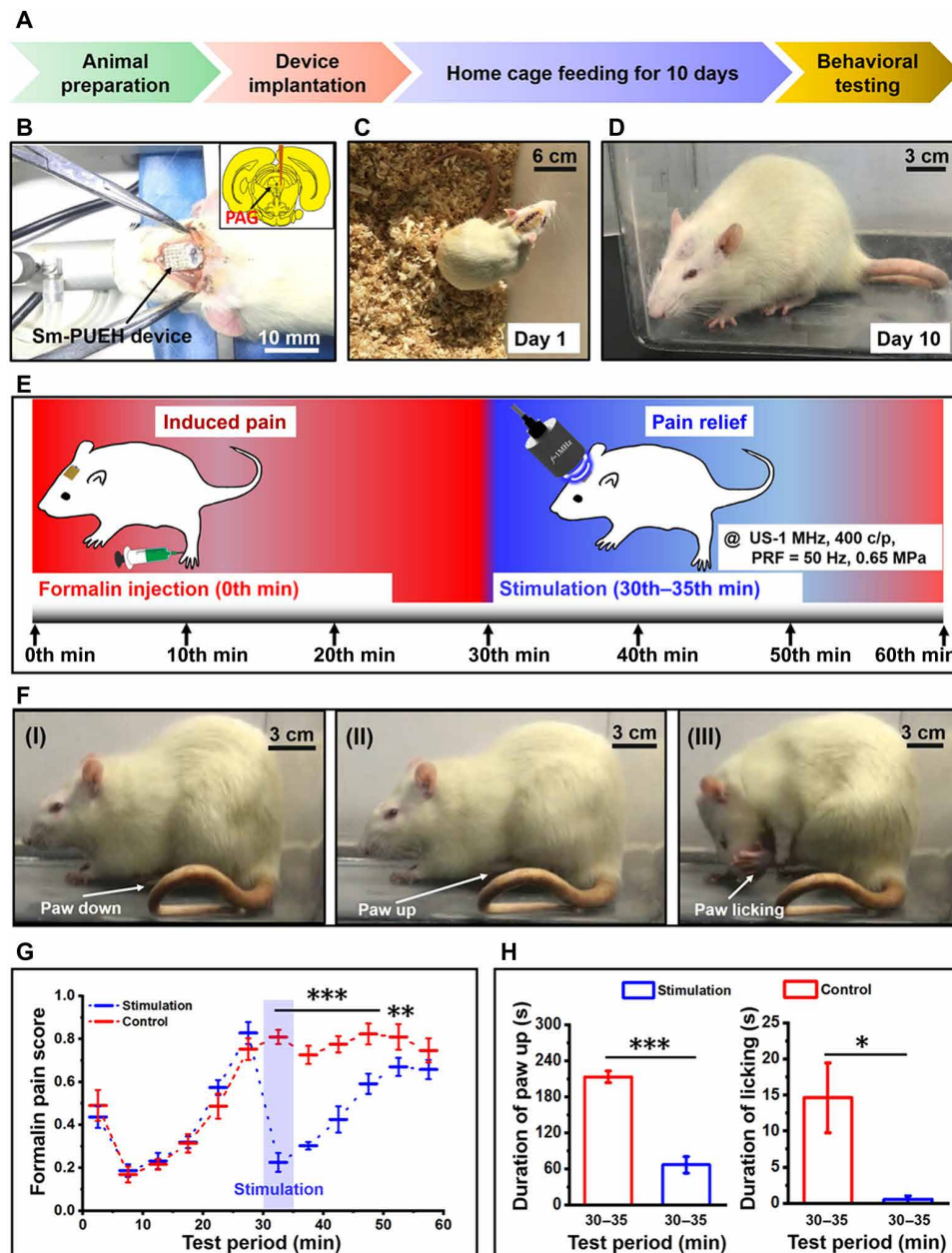
Fig. 6. Behavioral experiments in the rats with fully implanted Sm-PUEH device. (**A**) The timeline for the whole experimental procedure. (**B**) The device implantation. (**C**) The first day after implantation. (**D**) The 10th day after implantation. (**E**) Schematic diagram of behavioral experiments of Sm-PUEH device for analgesia application. Three-percent formalin (50 μl) is injected at the beginning, and US (US-400 c/p, *PRF* = 50 Hz, 0.65 MPa) is applied during the 30th to 35th min. (**F**) Three main behavioral responses of rats to formalin: (I) paw down, (II) paw up, and (III) paw licking, showing differential pain levels from no pain to the heaviest pain. (**G**) The weighted score comparison of formalin-induced pain between the stimulation group (*n* = 6) and the control group (*n* = 6). (**H**) Total time (seconds) of paw up (left) and paw licking (right) during the 30th to 35th min in formalin test. All data are presented as means ± SEM. *$P < 0.05$, **$P < 0.01$, and ***$P < 0.001$ versus control group.

26 times higher than the record value (60 mW/cm^2, 160 nW) in previous literature, respectively. In vivo, our device can produce an instantaneous effective output power up to 280 μW under 1-MHz US with the intensity of 212 mW/cm^2, which is a record in PUEH devices. The observations of the rat's electrophysiological investigation and behavioral experiment demonstrate that our device does have the capability to realize DBS and immediately activate the PAG brain area for analgesia applications. These encouraging results suggest that such US-wireless energy harvesting technology is

a novel method for in vivo implantable biomedical devices. This study provides new insights into the development of implantable devices in the future.

MATERIALS AND METHODS
Sm-PUEH device fabrication
Sm-PMN-PT single crystal was grown by the modified Bridgman approach (*46*) and was lapped down to the thickness of 380 μm.

After Au/Cr (200/100 nm) electrodes were deposited on both sides of the polished single crystal by sputtering technology, the Sm-PMN-PT single crystal was cut into pieces with the size of 1 mm by 1 mm using a DAD323 dicing saw (DISCO, Saitama, Japan). To fabricate a flexible 6 × 6 array, copper stretchable electrodes were used to connect each element using E-Solder 3022 (Von Roll Isola, New Haven, CT, USA) as a binder (fig. S19). Last, the 6 × 6 array, rectifier circuit, and bipolar stimulating electrode (Plastics One Inc.) were connected and encapsulated in PDMS (Sylgard 184, Dow Corning Corp.).

Characterization for material and device
An impedance analyzer (4294A, Agilent) was used to characterize the impedance spectra of the Sm-PMN-PT single crystal. The input sinusoidal signal of the US transmitter was provided by a function generator (AFG3252C, Tektronix), and the power was then amplified by a power amplifier (AG1020, US T&C). A digital oscilloscope (DSO-x3024a, Agilent) was used to measure the output voltage generated by the Sm-PUEH device. A hydrophone probe (Precision Acoustic, UK) was adopted to measure the output sound pressure of the US transducer in a DI water tank, and the pulse intensity integral (PII), the spatial-peak temporal average intensity (I_{SPTA}), and the mechanical index (MI) are defined as (72)

$$PII = \int \frac{P^2(t)}{Z_0} dt \qquad (3)$$

$$I_{SPTA} = PII \times PRF \qquad (4)$$

$$MI = \frac{p_r}{\sqrt{f}} \qquad (5)$$

where P is the instantaneous peak pressure, Z_0 is the characteristic acoustic impedance in pascal-second per meter defined as ρc, where ρ is the density of the medium and c is the speed of sound in the medium; p_r is the peak negative pressure of the US in megapascals; and f is the center frequency of the US transducer in megahertz.

Electrolytic test
One bipolar stimulating electrode was immersed in normal saline, and a microscope (XD-202, Nanjing Jiangnan Yongxin optics Co. Ltd) was used to observe the bubbles generated by the electrolysis at the tip. During the 1-MHz US irradiation (400 c/p, 0.65 MPa), the PRF was modulated. The duration of stimulation was recorded when bubbles appear at the electrode tip, and each datapoint was repeated four times.

Animal surgery
Thirty-eight Sprague-Dawley male rats weighing 300 to 450 g were used in this study. All procedures were approved by the Institutional Animal Care and Use Committee at the Huazhong University of Science and Technology in Wuhan, China. The rats were housed in a room with controllable temperature and humidity, the light/dark cycle was 12 hours, and food and water were provided at will. During the entire surgical operation and electrophysiological experiments, the rats were first anesthetized with 5% isoflurane in oxygen and then placed on a standard stereotaxic apparatus with 1.5 to 3% isoflurane for maintenance. A feedback heating pad was used to keep the rats at a stable body temperature when the experiments were carried out.

The PAG activation by the Sm-PUEH device
The stimulating and recording electrodes (a diameter of 0.01 inch with a very small impedance of 0.01 ohm, Plastics One Inc.) were inserted into the PAG brain area of the rat with ~1.5 mm of distance. The positioning method was offset 7 mm from the bregma of the skull to the tail, offset 0.5 mm from the midline to the right side, and depth downward from the brain surface 5.5 mm (73). One screw fixed on the skull connecting to a wire was used as reference and ground. Under an applied US (US-400 c/p, PRF = 50 Hz), the Sm-PUEH device generated electrical signals to stimulate the PAG brain area; meanwhile, the LFP signals were recorded by a wireless module (SiChuan NeoSource BioTektronics Limited). Last, to detect the periodic change of the signals activated by the PAG stimulation easily, the signal data were imported into Spike2 software (Cambridge Electronics Design Ltd., UK) and processed with a high-pass filter.

Electrophysiological experiment under anesthesia
In this experiment, 16 male Sprague-Dawley rats were randomly divided into two groups: the control group ($n = 8$) and the stimulation group ($n = 8$). A 3- to 4-cm laminectomy was performed on the back of the rat to expose the lumbosacral segment of the rat's spinal cord. The spinal cord was fixed in a stereotaxic frame (RWD Life Science Co. Ltd) and protected with mineral oil. An electrode (same as the one used in PAG recording) was inserted in the L5 spinal cord dorsal horn for recording the LFP activity. One clamp connecting to the surrounding skin was used as reference and ground. The stimulating electrode was placed in the PAG area. In each experiment, no treatments were done for the first 5 min, and the baseline signal was recorded. At time = 0, 50 μl of 3% formalin solution was injected into the left hindpaw. In the stimulation group, US (US-400 c/p, PRF = 50 Hz) stimulation for 5 min with an interval (on 3 s and off 3 s) was carried out at the 30th min, while there was no stimulation for the control group. In our study, the effective power to activate the PAG brain area was about 240 to 280 μW after the systematic optimization. The ideal power to activate the PAG brain area was about 280 μW, where the current was 175 μA equivalently.

Behavioral experiments
In this experiment, 12 Sprague-Dawley male rats were randomly divided into the stimulation group ($n = 6$) and the control group ($n = 6$) for device implantation. The brain on the PAG region was exposed by opening the skull of the rat, and the bipolar stimulation electrode was then placed in the PAG. The device was fixed on the skull with dental cement and three to four anchor screws. Last, the animal skin was sutured, and the device was completely enclosed under the skin. Buprenorphine (1 mg/kg) was given as an analgesic. The sutures were removed on the fifth day (after the wound had scabbed). At the 10th day, the hair of the rat brain was shaved before the experiment. During the experiment, 50 μl of 3% formalin was injected into the left hindpaw. US irradiation was performed at the 30th min for 5 min with an interval (on 3 s and off 3 s).

The pain behavior of the rat can be classified into three levels: level 1, the injected paw of the rat touches the ground (paw down); level 2, the rat lifts the injected paw from the ground (paw up); and level 3, the rat licks the injected paw (paw licking). After formalin injection, the rats were placed in an observation cage for pain measurement using a double-blind method. The time (in second) spent on the three-level behavior of the rat was recorded within 60 min,

and weighted pain score was then calculated with a period of 5 min (time bin = 5 min) with the following method (*74*)

$$Pain\ score\ =\ \frac{0 \times T1 + 1 \times T2 + 2 \times T3}{300} \tag{6}$$

where *T1*, *T2*, and *T3* represent levels 1, 2, and 3, respectively.

Biocompatibility studies in vivo

Six rats were implanted with the Sm-PUEH device, and two untreated rats were used as the control group (naive animals). One, 2, and 4 weeks after the surgery, the rats were euthanized. The scalp tissue above the device with four squares (5 mm by 5 mm for each square) and the brain were extracted and then fixed in 3.7% formaldehyde for 24 hours. The paraffin-embedded skin and brain were sectioned using a pathological microtome (Leica, RM2016) (4 μm). The sliced sections were then stained with hematoxylin and eosin and observed using a digital microscope. The thickness of loose areola tissue was measured and analyzed (fig. S3).

Statistical analysis

The collected raw data were imported into Spike2. Power spectrum analysis was performed using MATLAB 2012a (delta, 0 to 3 Hz; theta, 4 to 7 Hz; alpha, 8 to 12 Hz; beta, 13 to 30 Hz; and gamma, 31 to 100 Hz). A mixed analysis of variance (ANOVA) with least significant difference post hoc was used to test the significant difference between LFP power and behavior. A paired *t* test was applied to test the difference of duration of paw up and paw licking between stimulation and control groups. SPSS was applied to test statistical significance. All data are presented as means ± SEM.

SUPPLEMENTARY MATERIALS

Supplementary material for this article is available at https://science.org/doi/10.1126/sciadv.abk0159

REFERENCES AND NOTES

1. K. Bazaka, M. V. Jacob, Implantable devices: Issues and challenges. *Electronics* **2**, 1–34 (2013).
2. E. Meng, R. Sheybani, Insight: Implantable medical devices. *Lab Chip* **14**, 3233–3240 (2014).
3. P. Li, G. H. Lee, S. Y. Kim, S. Y. Kwon, H. R. Kim, S. Park, From diagnosis to treatment: Recent advances in patient-friendly biosensors and implantable devices. *ACS Nano* **15**, 1960–2004 (2021).
4. A. L. Benabid, S. Chabardes, J. Mitrofanis, P. Pollak, Deep brain stimulation of the subthalamic nucleus for the treatment of Parkinson's disease. *Lancet Neurol.* **8**, 67–81 (2009).
5. W. C. Koller, K. E. Lyons, S. B. Wilkinson, A. I. Troster, R. Pahwa, Long-term safety and efficacy of unilateral deep brain stimulation of the thalamus in essential tremor. *Mov. Disord.* **16**, 464–468 (2001).
6. Z. H. T. Kiss, K. Doig-Beyaert, M. Eliasziw, J. Tsui, A. Haffenden, O. Suchowersky, The Canadian multicentre study of deep brain stimulation for cervical dystonia. *Brain* **130**, 2879–2886 (2007).
7. L. A. Frizon, E. A. Yamamoto, S. J. Nagel, M. T. Simonson, O. Hogue, A. G. Machado, Deep brain stimulation for pain in the modern era: A systematic review. *Clin. Neurosurg.* **86**, 191–202 (2020).
8. M. L. Welter, J. L. Houeto, S. Thobois, B. Bataille, M. Guenot, Y. Worbe, A. Hartmann, V. Czernecki, E. Bardinet, J. Yelnik, S. T. du Montcel, Y. Agid, M. Vidailhet, P. Cornu, A. Tanguy, S. Ansquer, N. Jaafari, E. Poulet, G. Serra, P. Burbaud, E. Cuny, B. Aouizerate, P. Pollak, S. Chabardes, M. Polosan, M. Borg, D. Fontaine, B. Giordana, S. Raoul, T. Rouaud, A. Sauvaget, I. Jalenques, C. Karachi, L. Mallet, P. Derkinderen, A. Bissery, H. Oya, A. Buot, M. Hajji, D. Dormont, F. Durif, C. Fauchon, F. Rondepierre, P. Derost, M. A. Kombo, A. Krainik, P. Krack, B. Piallat, H. Klinger, E. Broussolle, P. Damier, M. N. Magnie-Mauro, I. Benatru, A. Fradet, E. Dugast, A. Ouerdani, E. Rabois, M. Quintin, S. Palfi, Anterior pallidal deep brain stimulation for Tourette's syndrome: A randomised, double-blind, controlled trial. *Lancet Neurol.* **16**, 610–619 (2017).
9. X. L. Zhong, J. T. Yu, Q. Zhang, N. D. Wang, L. Tan, Deep brain stimulation for epilepsy in clinical practice and in animal models. *Brain Res. Bull.* **85**, 81–88 (2011).
10. K. Ashkan, P. Rogers, H. Bergman, I. Ughratdar, Insights into the mechanisms of deep brain stimulation. *Nat. Rev. Neurol.* **13**, 548–554 (2017).
11. O. Jitkritsadakul, R. Bhidayasiri, S. K. Kalia, M. Hodaie, A. M. Lozano, A. Fasano, Systematic review of hardware-related complications of deep brain stimulation: Do new indications pose an increased risk? *Brain Stimul.* **10**, 967–976 (2017).
12. H. Cagnan, T. Denison, C. McIntyre, P. Brown, Emerging technologies for improved deep brain stimulation. *Nat. Biotechnol.* **37**, 1024–1033 (2019).
13. M. Y. Oh, A. Abosch, S. H. Kim, A. E. Lang, A. M. Lozano, Long-term hardware-related complications of deep brain stimulation. *Neurosurgery* **50**, 1268–1274; discussion 1274-1276 (2002).
14. G. Fernández-Pajarín, A. Sesar, B. Ares, J. L. Relova, E. Arán, M. Gelabert-González, A. Castro, Delayed complications of deep brain stimulation: 16-year experience in 249 patients. *Acta Neurochir.* **159**, 1713–1719 (2017).
15. M. Y. Oh, M. Hodaie, S. H. Kim, A. Alkhani, A. E. Lang, A. M. Lozano, Deep brain stimulator electrodes used for lesioning: Proof of principle. *Neurosurgery* **49**, 363–367; discussion 367-369 (2001).
16. R. J. Coffey, Deep brain stimulation devices: A brief technical history and review. *Artif. Organs* **33**, 208–220 (2009).
17. M. Hariz, Battery obsolescence, industry profit and deep brain stimulation. *Acta Neurochir.* **161**, 2047–2048 (2019).
18. D. G. Hargreaves, S. J. Drew, R. Eckersley, Kirschner wire pin tract infection rates: A randomized controlled trial between percutaneous and buried wires. *J. Hand Surg. Am.* **29**, 374–376 (2004).
19. F. W. Horlbeck, F. Mellert, J. Kreuz, G. Nickenig, J. O. Schwab, Real-world data on the lifespan of implantable cardioverter-defibrillators depending on manufacturers and the amount of ventricular pacing. *J. Cardiovasc. Electrophysiol.* **23**, 1336–1342 (2012).
20. A. Singer, S. Dutta, E. Lewis, Z. Chen, J. C. Chen, N. Verma, B. Avants, A. K. Feldman, J. O'Malley, M. Beierlein, C. Kemere, J. T. Robinson, Magnetoelectric materials for miniature, wireless neural stimulation at therapeutic frequencies. *Neuron* **107**, 631–643 (2020).
21. D. K. Piech, B. C. Johnson, K. Shen, M. M. Ghanbari, K. Y. Li, R. M. Neely, J. E. Kay, J. M. Carmena, M. M. Maharbiz, R. Muller, A wireless millimetre-scale implantable neural stimulator with ultrasonically powered bidirectional communication. *Nat. Biomed. Eng.* **4**, 207–222 (2020).
22. L. Jiang, Y. Yang, Y. Chen, Q. Zhou, Ultrasound-induced wireless energy harvesting: From materials strategies to functional applications. *Nano Energy* **77**, 105131 (2020).
23. W. F. Pritchard, R. F. Carey, U.S. Food and Drug Administration and regulation of medical devices in radiology. *Radiology* **205**, 27–36 (1997).
24. J. C. Lin, A new IEEE standard for safety levels with respect to human exposure to radio-frequency radiation. *IEEE Antennas Propag. Mag.* **48**, 157–159 (2006).
25. C. Y. Kim, M. J. Ku, R. Qazi, H. J. Nam, J. W. Park, K. S. Nam, S. Oh, I. Kang, J. H. Jang, W. Y. Kim, J. H. Kim, J. W. Jeong, Soft subdermal implant capable of wireless battery charging and programmable controls for applications in optogenetics. *Nat. Commun.* **12**, 535 (2021).
26. D. R. Agrawal, Y. Tanabe, D. Weng, A. Ma, S. Hsu, S. Y. Liao, Z. Zhen, Z. Y. Zhu, C. Sun, Z. Dong, F. Yang, H. F. Tse, A. S. Y. Poon, J. S. Ho, Conformal phased surfaces for wireless powering of bioelectronic microdevices. *Nat. Biomed. Eng.* **1**, 0043 (2017).
27. S. Il Park, D. S. Brenner, G. Shin, C. D. Morgan, B. A. Copits, H. U. Chung, M. Y. Pullen, K. N. Noh, S. Davidson, S. J. Oh, J. Yoon, K. I. Jang, V. K. Samineni, M. Norman, J. G. Grajales-Reyes, S. K. Vogt, S. S. Sundaram, K. M. Wilson, J. S. Ha, R. Xu, T. Pan, T. Il Kim, Y. Huang, M. C. Montana, J. P. Golden, M. R. Bruchas, R. W. Gereau, J. A. Rogers, Soft, stretchable, fully implantable miniaturized optoelectronic systems for wireless optogenetics. *Nat. Biotechnol.* **33**, 1280–1286 (2015).
28. R. Hinchet, H. J. Yoon, H. Ryu, M. K. Kim, E. K. Choi, D. S. Kim, S. W. Kim, Transcutaneous ultrasound energy harvesting using capacitive triboelectric technology. *Science* **365**, 491–494 (2019).
29. G. Yao, L. Kang, J. Li, Y. Long, H. Wei, C. A. Ferreira, J. J. Jeffery, Y. Lin, W. Cai, X. Wang, Effective weight control via an implanted self-powered vagus nerve stimulation device. *Nat. Commun.* **9**, 5349 (2018).
30. G. Yao, D. Jiang, J. Li, L. Kang, S. Chen, Y. Long, Y. Wang, P. Huang, Y. Lin, W. Cai, X. Wang, Self-activated electrical stimulation for effective hair regenerationvia a wearable omnidirectional pulse generator. *ACS Nano* **13**, 12345–12356 (2019).
31. A. G. Fowler, S. O. R. Moheimani, S. Behrens, An omnidirectional MEMS ultrasonic energy harvester for implanted devices. *J. Microelectromech. Syst.* **23**, 1454–1462 (2014).
32. M. Deterre, S. Risquez, B. Bouthaud, R. D. Molin, M. Woytasik, E. Lefeuvre, Multilayer out-of-plane overlap electrostatic energy harvesting structure actuated by blood pressure for powering intra-cardiac implants. *J. Phys. Conf. Ser.* **476**, 012039 (2013).
33. Z. Xu, X. Wan, X. Mo, S. Lin, S. Chen, J. Chen, Y. Pan, H. Zhang, H. Jin, J. Duan, L. Huang, L.-B. Huang, J. Xie, F. Yi, B. Hu, J. Zhou, Electrostatic assembly of laminated transparent piezoelectrets for epidermal and implantable electronics. *Nano Energy* **89**, 106450 (2021).

34. S. El Ichi-Ribault, J. P. Alcaraz, F. Boucher, B. Boutaud, R. Dalmolin, J. Boutonnat, P. Cinquin, A. Zebda, D. K. Martin, Remote wireless control of an enzymatic biofuel cell implanted in a rabbit for 2 months. *Electrochim. Acta* **269**, 360–366 (2018).

35. N. Mano, F. Mao, A. Heller, Characteristics of a miniature compartment-less glucose-O_2 biofuel cell and its operation in a living plant. *J. Am. Chem. Soc.* **125**, 6588–6594 (2003).

36. D. Rozgić, D. Marković, A miniaturized 0.78-mW/cm2 autonomous thermoelectric energy-harvesting platform for biomedical sensors. *IEEE Trans. Biomed. Circuits Syst.* **11**, 773–783 (2017).

37. M. Strasser, R. Aigner, C. Lauterbach, T. F. Sturm, M. Franosch, G. K. M. Wachutka, Micromachined CMOS thermoelectric generators as on-chip power supply. *Sensors Actuators A Phys.* **114**, 362–370 (2004).

38. J. Jeong, J. Jung, D. Jung, J. Kim, H. Ju, T. Kim, J. Lee, An implantable optogenetic stimulator wirelessly powered by flexible photovoltaics with near-infrared (NIR) light. *Biosens. Bioelectron.* **180**, 113139 (2021).

39. C. Vargas-Estevez, A. Blanquer, G. Murillo, M. Duque, L. Barrios, C. Nogués, E. Ibañez, J. Esteve, Electrical stimulation of cells through photovoltaic microcell arrays. *Nano Energy* **51**, 571–578 (2018).

40. X. Wang, J. Song, J. Liu, L. W. Zhong, Direct-current nanogenerator driven by ultrasonic waves. *Science* **316**, 102–105 (2007).

41. S. Islam, A. Kim, Ultrasonic energy harvesting scheme for implantable active stent. *IMBioc 2018–2018 IEEE/MTT-S Int. Microw. Biomed. Conf.* 70–72 (2018).

42. Q. Shi, T. Wang, C. Lee, MEMS based broadband piezoelectric ultrasonic energy harvester (PUEH) for enabling self-powered implantable biomedical devices. *Sci. Rep.* **6**, 24946 (2016).

43. Z. Yang, D. Zeng, H. Wang, C. Zhao, J. Tan, Harvesting ultrasonic energy using 1-3 piezoelectric composites. *Smart Mater. Struct.* **24**, 075029 (2015).

44. L. Jiang, Y. Yang, R. Chen, G. Lu, R. Li, D. Li, M. S. Humayun, K. K. Shung, J. Zhu, Y. Chen, Q. Zhou, Flexible piezoelectric ultrasonic energy harvester array for bio-implantable wireless generator. *Nano Energy* **56**, 216–224 (2019).

45. L. Jiang, Y. Yang, R. Chen, G. Lu, R. Li, J. Xing, K. K. Shung, M. S. Humayun, J. Zhu, Y. Chen, Q. Zhou, Ultrasound-induced wireless energy harvesting for potential retinal electrical stimulation application. *Adv. Funct. Mater.* **29**, 1902522 (2019).

46. F. Li, M. J. Cabral, B. Xu, Z. Cheng, E. C. Dickey, J. M. LeBeau, J. Wang, J. Luo, S. Taylor, W. Hackenberger, L. Bellaiche, Z. Xu, L. Chen, T. R. Shrout, S. Zhang, Giant piezoelectricity of Sm-doped Pb($Mg_{1/3}Nb_{2/3}$)O_3-$PbTiO_3$ single crystals. *Science* **364**, 264–268 (2019).

47. H. F. Tiersten, *Linear Piezoelectric Plate Vibrations* (Plenum Press, 1969).

48. J. Yang, H. Zhou, Y. Hu, Q. Jiang, Performance of a piezoelectric harvester in thickness-stretch mode of a plate. *IEEE Trans. Ultrason. Ferroelectr. Freq. Control* **52**, 1872–1876 (2005).

49. M. Hayner, K. Hynynen, Numerical analysis of ultrasonic transmission and absorption of oblique plane waves through the human skull. *J. Acoust. Soc. Am.* **110**, 3319–3330 (2001).

50. Y. Tufail, A. Matyushov, N. Baldwin, M. L. Tauchmann, J. Georges, A. Yoshihiro, S. I. H. Tillery, W. J. Tyler, Transcranial pulsed ultrasound stimulates intact brain circuits. *Neuron* **66**, 681–694 (2010).

51. H. Azhari, *Basics of Biomedical Ultrasound for Engineers* (John Wiley & Sons Inc., 2010).

52. S. Xu, Y. Zhang, J. Cho, J. Lee, X. Huang, L. Jia, J. A. Fan, Y. Su, J. Su, H. Zhang, H. Cheng, B. Lu, C. Yu, C. Chuang, T. Il Kim, T. Song, K. Shigeta, S. Kang, C. Dagdeviren, I. Petrov, P. V. Braun, Y. Huang, U. Paik, J. A. Rogers, Stretchable batteries with self-similar serpentine interconnects and integrated wireless recharging systems. *Nat. Commun.* **4**, 1543 (2013).

53. H. Hu, X. Zhu, C. Wang, L. Zhang, X. Li, S. Lee, Z. Huang, R. Chen, Z. Chen, C. Wang, Y. Gu, Y. Chen, Y. Lei, T. Zhang, N. H. Kim, Y. Guo, Y. Teng, W. Zhou, Y. Li, A. Nomoto, S. Sternini, Q. Zhou, M. Pharr, F. L. di Scalea, S. Xu, Stretchable ultrasonic transducer arrays for three-dimensional imaging on complex surfaces. *Sci. Adv.* **4**, eaar3979 (2018).

54. J. A. Rogers, T. Someya, Y. Huang, Materials and mechanics for stretchable electronics. *Science* **327**, 1603–1607 (2010).

55. S. M. Won, L. Cai, P. Gutruf, J. A. Rogers, Wireless and battery-free technologies for neuroengineering. *Nat. Biomed. Eng.* (2021).

56. Y. Zhu, S. O. R. Moheimani, M. R. Yuce, A 2-DOF MEMS ultrasonic energy harvester. *IEEE Sensors J.* **11**, 155–161 (2011).

57. A. G. Fowler, S. O. R. Moheimani, S. Behrens, A 3-DoF MEMS ultrasonic energy harvester. *Proc. IEEE Sensors*, 1–4 (2012).

58. D. R. Merrill, M. Bikson, J. G. R. Jefferys, Electrical stimulation of excitable tissue: Design of efficacious and safe protocols. *J. Neurosci. Methods* **141**, 171–198 (2005).

59. S. D. Mathias, M. Kuppermann, R. F. Liberman, R. C. Lipschutz, J. F. Steege, Chronic pelvic pain: Prevalence, health-related quality of life, and economic correlates. *Obstet. Gynecol.* **87**, 321–327 (1996).

60. P. H. Rosenberger, P. Jokl, J. Ickovics, Psychosocial factors and surgical outcomes: An evidence-based literature review. *J. Am. Acad. Orthop. Surg.* **14**, 397–405 (2006).

61. F. M. Blyth, G. J. Macfarlane, M. K. Nicholas, The contribution of psychosocial factors to the development of chronic pain: The key to better outcomes for patients? *Pain* **129**, 8–11 (2007).

62. K. P. Jordan, E. Thomas, G. Peat, R. Wilkie, P. Croft, Social risks for disabling pain in older people: A prospective study of individual and area characteristics. *Pain* **137**, 652–661 (2008).

63. C. Naumann, S. Erdine, A. Koulousakis, J. P. Van Buyten, M. Schuchard, Drug adverse events and system complications of intrathecal opioid delivery for pain: Origins, detection, manifestations, and management. *Neuromodulation* **2**, 92–107 (1999).

64. W. Winkelmuller, K. Burchiel, J. P. Van Buyten, Intrathecal opioid therapy for pain: Efficacy and outcomes. *Neuromodulation* **2**, 67–76 (1999).

65. R. Levine, M. M. Morgan, J. T. Cannon, J. C. Liebeskind, Stimulation of the periaqueductal gray matter of the rat produces a preferential ipsilateral antinociception. *Brain Res.* **567**, 140–144 (1991).

66. B. H. Lee, S. H. Park, R. Won, Y. G. Park, J. H. Sohn, Antiallodynic effects produced by stimulation of the periaqueductal gray matter in a rat model of neuropathic pain. *Neurosci. Lett.* **291**, 29–32 (2000).

67. T. Ativanichayaphong, J. W. He, C. E. Hagains, Y. B. Peng, J. C. Chiao, A combined wireless neural stimulating and recording system for study of pain processing. *J. Neurosci. Methods* **170**, 25–34 (2008).

68. K. S. Lee, Y. H. Huang, C. T. Yen, Periaqueductal gray stimulation suppresses spontaneous pain behavior in rats. *Neurosci. Lett.* **514**, 42–45 (2012).

69. C. Zuo, X. Yang, Y. Wang, C. E. Hagains, A. L. Li, Y. B. Peng, J. C. Chiao, A digital wireless system for closed-loop inhibition of nociceptive signals. *J. Neural Eng.* **9**, 056010 (2012).

70. Y. B. Peng, Q. Lin, W. D. Willis, Effects of GABA and glycine receptor antagonists on the activity and PAG-induced inhibition of rat dorsal horn neurons. *Brain Res.* **736**, 189–201 (1996).

71. D. D. Price, Central neural mechanisms that interrelate sensory and affective dimensions of pain. *Mol. Interv.* **2**, 392–403, 339 (2002).

72. National Electrical Manufacturers Association, *Acoustic Output Measurement Standard for Diagnostic Ultrasound Equipment* (National Electrical Manufacturers Association, 2004).

73. G. Paxinos, C. Watson, *The Rat Brain in Stereotaxic Coordinates Hard Cover Edition* (Academic Press, 2007).

74. C. J. LaBuda, R. Donahue, P. N. Fuchs, Enhanced formalin nociceptive responses following L5 nerve ligation in the rat reveals neuropathy-induced inflammatory hyperalgesia. *Pain* **94**, 59–63 (2001).